Eur. Phys. J. D **40**, 181–193 (2006)
DOI: 10.1140/epjd/e2006-00153-8

THE EUROPEAN PHYSICAL JOURNAL D

Lineshapes of the even $mp^5_{1/2}n(p'/f')$ autoionizing resonances of Ar, Kr and Xe

I.D. Petrov[1,2], T. Peters[2], T. Halfmann[2], S. Aloïse[3], P. O'Keeffe[3], M. Meyer[3,4], V.L. Sukhorukov[1,2,a], and H. Hotop[2]

[1] Rostov State University of TC, 344038 Rostov-on-Don, Russia
[2] Technische Universität Kaiserslautern, 67653 Kaiserslautern, Germany
[3] LURE, Centre Universitaire Paris-Sud, Bâtiment 209D, 91898 Orsay Cedex, France
[4] LIXAM, Centre Universitaire Paris-Sud, Bâtiment 350, 91405 Orsay Cedex, France

Received 29 March 2006 / Received in final form 25 May 2006
Published online 30 June 2006 –

Abstract. The even parity $mp^5_{1/2}np'$ and $mp^5_{1/2}nf'$ autoionizing resonances of Ar, Kr, and Xe ($m = 3, 4, 5$) were investigated experimentally and theoretically by one-photon excitation from lower-lying intermediate levels. In particular, high resolution measurements for the Ar(nf'), Kr($12p', 8f'$), and Xe($8p'$) resonances are reported; lineshape parameters for these resonances have been derived by a Fano-type analysis, thus yielding reduced resonance widths. The experimental spectra and the resonance parameters are compared with theoretical calculations which are based on the configuration interaction Pauli–Fock approach including core polarization. The measured and calculated lineshapes are in good agreement. In addition, theoretical predictions are presented for other resonances, which have not yet been observed experimentally, and some systematic trends are elucidated.

PACS. 32.80.Fb Photoionization of atoms and ions – 32.80.Dz Autoionization – 31.25.-v Electron correlation calculations for atoms and molecules

1 Introduction

Excitation processes in the rare gas atoms Ne, Ar, Kr and Xe (Rg) with energies between the two lowest ionization thresholds $mp^5_{3/2}$ and $mp^5_{1/2}$ ($m = 2$–5) are dominated by resonances attributed to $mp^5_{1/2}n\ell'[K']_J$ autoionizing Rydberg states (ARS). Starting with the pioneering work of Beutler [1] these resonances have been studied in some detail, both experimentally [2–7] and theoretically [8–15] (see also references in our previous paper [11]). Besides their characteristic lineshapes [16,17], the two main properties of the resonances which are derived from experimental spectra are the autoionization width Γ_n and the quantum defect μ_ℓ. The latter characterizes the resonance energy E_n through its binding energy relative to the $Rg^+ \left(^2P_{1/2}\right)$ threshold $I_{1/2}$: $I_{1/2} - E_n = \mathrm{Ry}/(n - \mu_\ell)^2$ (Ry is the Rydberg constant for the atom under consideration). The widths Γ_n depend strongly on the effective principal quantum number $n^* = n - \mu_\ell$ and on ℓ', but also – for given $n\ell'$ – on $K' = \ell' \pm 1/2$ and on the total angular momentum J. For a specified resonance series $n\ell'[K']_J$ the widths Γ_n are found to decrease as n^{*-3} at sufficiently high n^* [2,4,10–12]; correspondingly, most of the members of a particular resonance series can be characterized by a single quantity, called the reduced width Γ_r defined by $\Gamma_r = n^{*3}\Gamma_n$ [2,4,10–12], which varies somewhat with n^* at small n (see, e.g., [13]). The width of the ARS is determined by the interaction of the excited states with the continuum and with the nearby ARS of the same parity and total angular momentum J; these interactions are strongly affected by many-electron correlations.

Finding systematic trends and propensities in the dependence of the (reduced) resonance widths on the various quantum numbers is a desirable goal [4,10–12]. An important step in this direction was taken by Berkowitz [4], who surveyed the characteristics of ARS with configurations $p^{m-1}ns'$, nd', excited from the p^m ground state configuration, and provided qualitative discussions as well as simplified calculations of the Coulomb matrix elements describing the decay of the ARS. Much in the spirit of this work, we have carried out systematic Pauli–Fock calculations of the properties of the $n\ell'[K']_J$ ($\ell' = 0$–5) autoionizing resonances in Rg, and found an ℓ'^{-6} dependence of the reduced widths (valid for $\ell' \geq 3$) [11].

Ab initio calculations of the properties for ARS in the rare gas atoms are scarce [8–15,18–21]. As an important early example we note the efforts of Johnson and co-workers who applied the relativistic random phase approximation for the calculation of MQDT (multi-channel quantum defect theory) parameters for Ne [8], Ar, Kr and Xe [9]; based on these parameters, they used MQDT to predict the ns', $nd'J = 1$ autoionization spectra. The

[a] e-mail: vls@physik.uni-kl.de

resonance shapes were found to be in good agreement with the experimental data, but the predicted resonance widths were systematically larger (by factors between 1.5 and 2) than the corresponding experimental results (see, e.g., [10] for details regarding the $ns'\ J = 1$ series). This disagreement has recently prompted an extended consideration for the odd ARS [12,13]. It was found that the values for $\Gamma_r\,(ns'\ J = 1)$ are strongly influenced by mixing the ns'- and nd'-states; the values for $\Gamma_r\,(nd')$ are affected by both the interaction of the nd'-states through the autoionizing continuum and the sensitivity of the nd'-orbitals to details of the atomic potential.

The influence of many-electron effects on the lineshape of np'-resonances of Rg has been studied in recent work [14,15,22] by combining theoretical and experimental efforts. Following pioneering experimental work by Dunning et al. [3,23–26], the even $np'\ J = 1, 2$ ARS were investigated at much improved resolution by single-photon excitation from the metastable $\mathrm{Rg}(mp^5(m+1)s'\ {}^3P_0$, $mp^5(m+1)s\ {}^3P_2)$ levels in [14,27]. Resonant two-colour two-photon excitation of ground state rare gas atoms allowed measurements of all four np' series in Ne [15] and Xe [7,22] and, in particular, the $np'J = 0$ series which is of special theoretical interest. A strong influence of many-electron effects on the autoionizing lineshapes was revealed in [15,22]. We note that the lineshapes of the ARS may strongly depend on the level from which they were excited while the line widths and quantum defects of the ARS are independent of the particular excitation pathway.

In the present combined experimental and theoretical work, we address the autoionizing even-parity $n\,(p/f)'$ series of Ar, Kr and Xe. In the experimental study we used two different excitation schemes involving one-photon excitation from the metastable states and two-photon excitation from the ground state of the investigated atom. Theoretically, we build on our previous work, carried out within the Pauli–Fock approximation, and now include core polarization as well as different types of electron correlation effects. In this way improved many-electron calculations for the reduced widths and reliable predictions for the lineshapes of the even $n\ell'[K']_J\ (\ell' = 1, 3)$ resonances can be made. We provide a comparison between computed and measured lineshapes including available literature data.

The paper is organized as follows. In Section 2, we present the experimental procedures and the two different setups. In Section 3, we describe the technique of computing the lineshapes of the ARS taking into account many-electron correlations. These advanced many-electron calculations of the even parity $np'[K']_J$ and $nf'[K']_J$ resonances are compared with experimental data in Section 4. In Section 5, we conclude with a brief summary.

2 Experiment

In order to investigate the autoionizing Rydberg states (ARS) we used two different excitation schemes. In the first approach the $\mathrm{Ar}(nf')$ resonances were accessed by one-photon laser excitation from the metastable $3p^54s\ ({}^3P_2)$ level whereas the second scheme involved two-color double-resonant excitation of ground state Kr or Xe atoms, combining synchrotron and laser radiation.

2.1 Metastable atom experiment

A detailed description of the experimental set-up with respect to the preparation of the metastable states and detection of the ions can be found in reference [14]. Here only the most essential issues of the preparation are presented, while the laser system is discussed in some detail, since it is different from that described in reference [14].

Metastable $\mathrm{Ar}(3p^54s\ J_0 = 2, 0)$ atoms were prepared in an electron-injection seeded discharge in a pulsed supersonic beam. The majority of the metastable atoms (>80% [28,29]) were in the $J_0 = 2$ level. After passing through a skimmer and a condenser (to remove charged particles), the collimated metastable beam traversed a field-free volume between two electrodes. In the center of that region, it interacted with pulsed, ultraviolet (UV) radiation. 80 ns after the ultraviolet radiation pulse, the ions formed in the photoexcitation/ionization process were accelerated by a gated electric field of 2.8 $\mathrm{kV\,cm^{-1}}$ into a time-of-flight mass spectrometer and detected on a microsphere plate (El Mul Technologies).

To generate Fourier transform limited (FTL) UV laser pulses, the radiation of a continuous-wave dye laser system was used to seed a pulsed dye amplifier (PDA, Spectra Physics Quanta Ray PDA-1), pumped by FTL pulses of a frequency-doubled, injection-seeded Nd:YAG laser system (Spectra Physics Quanta Ray GCR-4). The cw dye laser system consists of a longitudinally and transversely single-mode dye laser (Coherent, Model 699, bandwidth 1 MHz) pumped by an Ar^+-laser (Spectra Physics Model 2030). The cw dye laser was tuned to wavelengths between 583 nm and 588 nm. The output of the PDA follows the wavelength given by the cw seed laser. The radiation pulses from the PDA were frequency doubled in a BBO crystal to yield ultraviolet radiation with photon energies between 34305 $\mathrm{cm^{-1}}$ and 34014 $\mathrm{cm^{-1}}$ and a FTL UV bandwidth of 0.004 $\mathrm{cm^{-1}}$. Pulse energies of typically 1 mJ in the UV were obtained and attenuated for the experiment to typical pulse energies of approximately 20 μJ with a pulse duration of 3.8 ns (FWHM). The beam diameter in the interaction region amounts to about 2 mm, corresponding to intensities of about 0.1 $\mathrm{MW/cm^2}$. At these intensities the ARS are not yet subject to significant power broadening as verified experimentally by measuring the line profile of the $\mathrm{Ar}(9f')$ ARS for different intensities. Raising the UV intensity by a factor of 80 (from 0.1 $\mathrm{MW/cm^2}$ to 8 $\mathrm{MW/cm^2}$ by increasing the pulse energy and by focussing) led to an increase of the effective resonance width by no more than 50%.

The transition energies from the metastable level to the $\mathrm{Ar}(9f', 10f')$ ARS were determined by measuring the wavelength of the visible radiation pulses of the PDA with a Fizeau-type wavemeter with a quoted uncertainty of

± 0.003 cm^{-1} (ATOS Lambdameter LM007) and by fitting Fano profiles to the experimentally measured peaks after calibrating the data with respect to the measured wavelength and scanning range. In order to determine the quantum defects of the ARS we used the value 35397.659(4) cm^{-1} for the ionization energy of Ar($4s\ ^3P_2$) with respect to the $Ar^+(^2P_{1/2})$ limit [30]. Accounting for the laser bandwidth, the wavelength uncertainty of the wavemeter, and the reliability in fixing the resonance position, we estimate the uncertainty of the resonance energy of the ARS to be approximately 0.01 cm^{-1}.

2.2 Two-color experiment

Two-color experiments have been performed at the SuperACO storage ring in Orsay (France) using a combination between synchrotron and laser radiation. For the excitation of the intermediate states in Kr($4p^5_{3/2}4d$ and $4p^5_{3/2}6s, J_0 = 1$) and Xe($5p^5_{3/2}7s, J_0 = 1$) monochromatized VUV synchrotron radiation from the SU5 beamline [31] was used, providing a photon flux of about 2×10^{10} photons/s within a bandpass of better than 2 meV in the energy region 5 eV $\leq h\nu$ (SR) $\leq$ 35 eV. Higher order light of the monochromator was efficiently suppressed by a differentially pumped high pressure gas cell in the front end of the beamline. The SR-excited atoms were subsequently excited to the autoionizing states by a continuous-wave, linear dye laser pumped by the 532 nm light of a frequency-doubled solid state laser (5W VERDI). Using Rhodamine 6G dye an average laser power of 800 mW and a spectral width of about 1.3 cm^{-1} was obtained at the maximum of the emission curve of the dye (595 nm). The laser and the synchrotron radiation were linearly polarized with high purity (P(SR) = 98% and P(laser) > 99%). For most of the experiments, in particular on Kr, a parallel orientation between both polarization vectors was chosen. Only for the reported experiments on Xe the polarization vector of the laser was rotated by means of a half-wave plate to a position corresponding to the magic angle, i.e. an angle of 54.7° between the polarization vector of the SR and the laser.

The laser light was introduced to the experimental chamber counterpropagating to the synchrotron beam. Both beams crossed an effusive gas jet in the acceptance volume of a time-of-flight analyzer. As a signature of the two-photon process we recorded the ion signal as a function of the laser wavelength, while the photon energy of the SR was tuned to the intermediate levels. The analysis of the ions was obtained by means of a magnetic sector field (0.1 T) at the end of the TOF drift tube. The mass resolution of this arrangement did not allow to separate the different isotopes of the rare gases, but enabled us to distinguish between the singly charged atomic ions and charged rare gas dimers, which are also formed in the interaction region. Within the wavelength range of the dye (580 nm $\leq \lambda$(laser) $\leq$ 620 nm) the autoionizing resonances np' and mf' with n = 11–13 and m = 7–11 could be studied, when exciting the Kr $4p^5(^2P_{3/2})4d\ J_0 = 1$ and $4p^5(^2P_{3/2})6s\ J_0 = 1$ levels at $h\nu$ = 12.35 eV and $h\nu$ = 12.38 eV, respectively. For Xe, only the $5p^5(^2P_{3/2})7s \rightarrow 5p^5(^2P_{1/2})8p'$ transitions are discussed in this paper. Other cases of resonant two-photon excitation of Xe can be found elsewhere [6,7,22]. All experiments have been performed using high purity (>99.9%) Kr and Xe gases. The background pressure in the experimental chamber was about 1×10^{-7} torr without gas load and about 3×10^{-5} torr during the experiments.

3 Theory

In order to compute the resonance parameters we used in the present paper the configuration interaction Pauli-Fock approach including core polarization, CIPFCP [12,32,33]. According to this technique the CI equations are built using atomic orbitals computed with accounting for the relativistic compression of the atomic core [29] and for core polarization [32,33]. Photoionization cross-sections — outlined below for the $4p^55s \rightarrow 4p^5\varepsilon\ell$ transition in krypton — were computed according to the following scheme:

$$\begin{array}{ccc} 4p^55s & \rightarrow & 4p^5\,(n/\varepsilon)\,\ell\ \ (\ell = \mathrm{p/f/h}) \\ \Updownarrow & & \Updownarrow \\ \left\{\begin{array}{l} 4p^4\varepsilon\ell\,\{\mathrm{s/d}\}\ \ (a) \\ 4s^14p^6\varepsilon\mathrm{p}\ \ (b) \\ 4p^5\,\{\mathrm{s/d}\}\ \ (c) \end{array}\right\} & & \left\{\begin{array}{l} 4p^45s\,\{\mathrm{s/d}\}\ \ (d) \\ 4s^14p^65s\ \ (e) \\ 4p^5\{\mathrm{p/f/h}\}\ (f) \end{array}\right\} \\ \textbf{ISCI} & & \textbf{FISCI} \end{array} \qquad (1)$$

where the horizontal arrow denotes the electric dipole interaction and the vertical double-arrows denote the Coulomb interaction. The outgoing continuum electron is characterized by its orbital angular momentum ℓ and its kinetic energy ε. A summation/integration over all states contained in the chain brackets was performed (continuum states were taken into account in a quasi-discrete manner). The basic configurations which contribute to the transition amplitude due to both initial state configuration interaction (ISCI) and final state configuration interaction (FISCI) are shown in scheme (1).

The photoionization cross-section for the initial state $|i_0\rangle = \left|4p^55s\,[K]_{J_0}\right\rangle$ was computed as:

$$\sigma^{j_c}_{i_0}(\omega) = \sum_J \sigma^{j_cJ}_{i_0}(\omega) \qquad (2)$$

$$\sigma^{j_cJ}_{i_0}(\omega) = \sum_{\ell,j} \sigma^{j_c\ell jJ}_{i_0}(\omega) \qquad (3)$$

$$\sigma^{j_c\ell jJ}_{i_0}(\omega) = \frac{4}{3\,(2J_0+1)}\pi^2\alpha a_0^2\omega^{\pm1} \times \left|\left\langle \overline{4p^5_{j_c}\varepsilon\ell_jJ}\,\|\mathbf{D}\|\,i_0\right\rangle\right|^2 \qquad (4)$$

where the signs (+) and (–) correspond to the length and velocity forms of the electric dipole operator $\mathbf{D}$, respectively; ω denotes the exciting photon energy in atomic units; $\alpha = 1/137.036$ is the fine structure constant; the square of the Bohr radius a_0^2 = 28.0028 Mb converts

atomic units for cross-sections to Mb $= 10^{-22}$ m^2; the partial cross-sections $\sigma_{i_0}^{j_c J}(\omega)$ and $\sigma_{i_0}^{j_c \ell j J}(\omega)$ are self explanatory. In the calculation of the dipole matrix elements, the correlations ($1a$–$1e$) are included via second order perturbation theory; the inclusion of the correlation ($1f$) is described below. For the sake of brevity we omitted in the text below the angular momentum of the core $j_c = 3/2$ in the notation of the total $\sigma_{i_0}(\omega)$ cross-section.

For completeness, we note that in two-photon experiments with two linearly polarized light beams the photoionization cross-section depends on the angle θ between the two electric vectors as follows (assuming that the intermediate level is not subject to hyperfine structure) [15]:

$$\begin{aligned}\sigma_{i_0}(\omega,\theta) = {} & \sigma_{i_0}^{J=0}(\omega)\left[1+2P_2(\cos\theta)\right] \\ & +\sigma_{i_0}^{J=1}(\omega)\left[1-P_2(\cos\theta)\right] \\ & +\sigma_{i_0}^{J=2}(\omega)\left[1+\frac{1}{5}P_2(\cos\theta)\right] \end{aligned} \quad (5)$$

where $P_2(\cos\theta)$ is the second Legendre polynomial. At the magic angle $\theta_{mag} = 54.7^\circ$ (where $P_2 = 0$) the cross-section $\sigma_{i_0}(\omega,\theta_{mag})$ is equal to the isotropic cross-section $\sigma_{i_0}(\omega)$ (Eq. (2)); this is also true in the presence of hyperfine structure. A direct comparison with the experimental results is therefore possible in the case of the Xe $8p'$ resonances (see below), because they have been recorded at the magic angle. But for the experiments on Kr the alignment of the intermediate state has to be taken into account when comparing the relative values of experimental and theoretical cross-sections.

The wave function of the final state $|\overline{4p^5_{3/2}\varepsilon\ell_j J}\rangle$ entering equation (4) contains both non-resonant and resonant parts accounting for all the even-parity ARS via the pathway ($1f$). This wave function was computed by applying the K-matrix technique [34] and the theory of interacting resonances in the complex calculus form [35] as:

$$\begin{aligned}\left|\overline{4p^5_{3/2}\varepsilon\ell_j J}\right\rangle = {} & \left|4p^5_{3/2}\varepsilon\ell_j J\right\rangle + \sum_i \frac{\left\langle \overline{i}\left|\mathbf{H}^{ee}\right|4p^5_{3/2}\varepsilon\ell_j J\right\rangle}{E-E^{(i)}} \\ & \times\left[\left|\overline{i}\right\rangle + \sum_\beta \int dE' \frac{\langle\beta E'\left|\mathbf{H}^{ee}\right|\overline{i}\rangle}{E-E'-\imath\delta}\left|\beta E'\right\rangle\right] \end{aligned} \quad (6)$$

where summation over all resonances $\left|\overline{i}\right\rangle$ and continua $|\beta E\rangle = \left|4p^5_{j_c}\varepsilon\ell_{j'}J\right\rangle$ is performed. The total energy E entering equation (6) is connected with the photoelectron energy ε and the threshold energy $IP_{\beta E}$ via the usual relation: $E = IP_{\beta E} + \varepsilon$. The 'non-resonant' continuum wave functions $|\beta E\rangle$ were computed using the K-matrix technique [34]. The wave functions of the resonances are modified via the interaction between continua and between resonances through continua:

$$\left|\overline{i}\right\rangle = \sum_m b_m^{(i)}\left|m\right\rangle. \quad (7)$$

The complex energies of the resonances $E^{(i)}$ and their wave functions (7) were obtained as the solution of the secular equation with a complex symmetric (and therefore non-Hermitian) matrix:

$$\sum_m \left[\left(E^{(i)}-E_m\right)\delta_{mm'} - \sum_\beta \int dE' \frac{\langle m\left|\mathbf{H}^{ee}\right|\beta E'\rangle\langle\beta E'\left|\mathbf{H}^{ee}\right|m'\rangle}{E-E'+\imath\delta}\right] b_m^{(i)} = 0 \quad (8)$$

where $b_m^{(n)}$ are complex numbers; $|m\rangle$ denotes the PF wave functions of the ARS. The complex energy of each resonance determines its position E_i and width Γ_i as

$$E_i = \mathrm{Re}E^{(i)}, \qquad \Gamma_i = -2\mathrm{Im}E^{(i)}. \quad (9)$$

The latter parameters determine the quantities, which only weakly depend on the principal quantum number n, i.e. the quantum defects μ and the reduced widths Γ_r via the following equations [4]:

$$E_i = E_i^\infty - \mathrm{Ry}/(n-\mu)^2, \qquad \Gamma_r = \Gamma_i(n-\mu)^3 \quad (10)$$

where E_i^∞ is the energy of the threshold to which the ARS converge.

The wave function (7) allows one to compute the complex transition amplitude $D^{(i)}$ and Fano parameters [16,17] for the resonance $|\overline{i}\rangle$ as:

$$\begin{aligned} D^{(i)} = {} & \langle\overline{i}\left|\mathbf{D}\right|i_0\rangle \\ & + \sum_\beta \int dE' \frac{\langle\overline{i}\left|\mathbf{H}^{ee}\right|\beta E'\rangle\langle\beta E'\left|\mathbf{H}^{ee}\right|i_0\rangle}{E-E'+\imath\delta}, \\ q_i = {} & -\frac{\mathrm{Re}D^{(i)}}{\mathrm{Im}D^{(i)}}, \quad \rho_i^2 = \frac{2\left(\mathrm{Im}D^{(i)}\right)^2}{\pi\Gamma_i\sigma_0} \end{aligned} \quad (11)$$

where the so-called non-resonant cross-section σ_0 is computed via equation (2) using the 'non-resonant' continuum wave functions $|4p^5_{3/2}\varepsilon\ell_j J\rangle$. With the parameters q_i, ρ_i^2, and σ_0 the photoionization cross-section (2) can be calculated by applying the following approximate formula [16,36]:

$$\sigma_{i_0}(\omega) = \sum_i \sigma_0\rho_i^2\left[\frac{(q_i+\varkappa_i)^2}{1+\varkappa_i^2}-1\right]+\sigma_0 \quad (12)$$

where $\varkappa_i$ is the reduced energy, referred to the respective resonance energy and given by $\varkappa_i = 2(E-E_i)/\Gamma_i$.

It is known that the Coulomb interaction entering scheme (1) should be computed with inclusion of many-electron effects [12]. The major part of these effects can be taken into account by computing scaling factors for the Slater integrals which enter the Coulomb matrix elements by the method described in [37,38]. These factors, computed in a way described earlier [12], are documented in Table 1. Scaling factors larger than 1 mean decreasing the interaction computed within the PF approach while the factors smaller than 1 mean increasing interaction. One can recognize from this table that on average (over the atoms and integrals) many-electron effects

Table 1. Scaling factors for the Slater integrals in column 1 are given with reference to scheme (1). The quantum numbers in column 2 correspond to the case of Kr.

Correlation	Integral	Ne	Ar	Kr	Xe
(a)	All	1.20	1.37	1.42	1.50
(d)	All	1.20	1.35	1.37	1.41
(b)	F^1(4s5s, 4pεp)	1.20	1.46	1.34	1.57
	G^1(4s5s, εp4p)	0.51	0.61	0.57	0.53
(e)	F^1(4p5s, 4sεp)	1.20	1.46	1.55	1.71
	G^0(5s4p, 4sεp)	1.07	0.99	1.00	0.99
(f)	F^2(4pεp, 4pε′p)	0.86	0.96	1.02	1.08
	G^0(4pεp, ε′p4p)	1.22	1.18	1.20	1.23
	G^2(4pεp, ε′p4p)	0.93	1.08	1.13	1.23
	F^2(4pεp, 4pε′f)	0.95	1.18	1.23	1.33
	G^2(4pεp, ε′f4p)	0.95	1.18	1.23	1.33
	F^2(4pεf, 4pε′f)	1.05	1.02	1.07	1.14
	G^2(4pεf, ε′f4p)	1.46	1.55	1.57	1.55
(c)	G^1(4p5s, εs4p)	1.25	1.15	1.20	1.28
	F^2(4p5s, 4pεd)	0.91	1.08	1.13	1.16
	G^1(4p5s, εd4p)	0.62	0.98	1.02	1.00
CP	All	1.15	1.25	1.26	1.26

decrease the Coulomb interaction. However, in some cases, e.g. G^1(4s5s, εp4p), many electron correlations can also increase the effective value of the Coulomb interaction considerably.

In the last line of Table 1 we list the scaling factors by which the ab-initio core polarization potentials were reduced computing the atomic orbitals by the technique described in our earlier work [32,33]. These factors were computed as a weighted average over the correlations determining the core polarization potential [37,38].

4 Results and discussion

Before we discuss the lineshapes of the even-parity ARS in Ar, Kr and Xe, excited from a variety of intermediate levels, we survey the results obtained for the reduced widths and quantum defects of these resonances. In Table 2 we compare the present CIPFCP results (Sect. 3) with the values of PF calculations [11] and selected experimental data (choosing those results which can be considered to be the most accurate and reliable). For completeness we also include results for Ne [14,15]. We note that the presently computed reduced widths for the $np'[K']_{1,2}$ resonances slightly differ from the values reported earlier [14] due to a more precise set of atomic orbitals, obtained in the self-consistent mp^5 atomic core (not in the core of the configuration $mp^5\,(m+1)\,s$ as in [14]).

The reduced widths of the nf'-resonances are found to rise with increasing atomic number Z. This trend is a consequence of an increasing density of the Rydberg electron inside the ionic core with rising Z, which causes an increase of the Slater integrals determining the autoionization rate. For the nf'-resonances many-electron correlations decrease the reduced widths of the nf'-resonances similar to the earlier findings for the odd parity ARS [13]. Therefore, the influence of many electron effects on the effective value of the Coulomb interaction is known as a 'correlational decrease'. For Xe two trends are observed which can be traced to the high spin-orbit splitting of the core as discussed elsewhere in more detail [11]: (i) a significant dependence of the reduced width on principal quantum number and (ii) the comparable values of the reduced width for the $K' = 5/2$ and $K' = 7/2$ ARS.

Experimental results for the narrow nf' resonances are still sparse. We note that the reduced widths obtained by four-photon excitation of ground state Ar, Kr, and Xe [39] are too high as a result of power broadening and therefore have been omitted. Accurate experimental values (uncertainty $\leq 10\%$) are available for $Xe(4f'[5/2]_2)$ [6], $Kr(nf'[5/2]_2, n = 7-9)$ and $Ar(nf'[5/2]_3,\ n = 9,10)$ (present experiments, see Tab. 2). In these cases the predicted CIPFCP values agree with the experimental data to within 20% or better. This is also true for the reduced width of $Xe(4f'[5/2]_3)$ for which we list a value obtained by re-analysis of the data in [26]. The recent results for the $Xe(4f'[7/2]_{3,4})$ ARS, obtained by Hanif et al. [27] with optogalvanic spectroscopy, suggest that the predicted reduced widths $\Gamma_r\,(4f'[7/2]_{3,4})$ are too high.

For the much broader np'-resonances the variation of the reduced widths with atomic number is rather weak except for the $np'[1/2]_0$ series where the reduced widths *decrease* from Ne to Xe due to the destructive interference between the direct $F^2(4pnp,\ 4p\varepsilon' p)$ and the exchange $G^0(4pnp,\ \varepsilon' p4p)$ Slater integrals. Not surprisingly, the largest influence of many-electron effects is found for the $np'[1/2]_0$ series for which the CIPFCP widths are on average two times higher than the PF values. The main reason for this increase is the interaction between the configurations $mp^5_{1/2}np'[1/2]_0$ and mp^6, which, within the conventional PF approach, describe the wave functions of the ARS and ground state, respectively. Inclusion of this interaction maintains also the orthogonality between the many-configurational wave functions of the ARS and ground state [15], which are non-orthogonal within the self-consistent PF approach. The experimental results for the reduced widths of the np'-resonances are found to agree with the predicted CIPFCP values to typically within 20%.

4.1 Rg (np′, nf′) resonances accessed from the metastable Rg ($^3P_{2,0}$) levels

Within the electric dipole selection rules for photoexcitation, the following ARS are accessible from the metastable states (we use the case of Kr as in scheme (1)):

$$4p^5_{1/2}5s'\ {}^3P_0 \xrightarrow{major} \left\{ \begin{array}{l} 4p^5_{1/2}np'[1/2]_1\ \text{(i)} \\ 4p^5_{1/2}np'[3/2]_1\ \text{(ii)} \end{array} \right\} \qquad (13)$$

Table 2. Quantum defects μ_ℓ and reduced widths Γ_r (cm^{-1}) of the np'/f' autoionizing Rydberg states in Ne, Ar, Kr and Xe.

Atom	Ref.	n	np' $K'=1/2$				np' $K'=3/2$			
			$J=0$		$J=1$		$J=1$		$J=2$	
			Γ_r	μ_ℓ	Γ_r	μ_ℓ	Γ_r	μ_ℓ	Γ_r	μ_ℓ
Ne	PF [a]	15	3335	0.745	1808	0.817	168	0.817	191	0.810
	CI [b]	13	6431	0.7634	2620	0.8397	249	0.8394	264	0.8317
	Exp [c]	13–15	5334(130)[d]	0.768(2)[d]	2550(150)	0.8403(8)	280(25)	0.8381(6)	320(20)[d]	0.8300(6)
Ar	PF	15	2184	1.565	3691	1.636	385	1.636	385	1.628
	CI	14	4507	1.599	4287	1.674	481	1.677	447	1.667
	Exp [e]	11–13	4050(600)	1.614						
	Exp [c]	13,14			3600(200)	1.675(3)			700(200)	1.668(3)
Kr	PF	20	1924	2.492	3960	2.565	691	2.565	671	2.557
	PF	9	1783	2.502	4064	2.571	668	2.571	649	2.563
	CI	14	3838	2.547	3886	2.607	795	2.619	597	2.602
	Exp [e]	8–10	4050(700)	2.558(4)					1080(420)	2.610(4)
	Exp [c]	12–14			2900(150)	2.613(3)	<1900	2.628(3)	450(200)	2.607(3)
	Exp [f]	12	3780(360)						680(115)	
Xe	PF	20	1856	3.399	4030	3.476	1711	3.476	1663	3.468
	PF	7	1450	3.433	4382	3.506	1738	3.506	1693	3.497
	CI	8	3197	3.504	3627	3.541	1424	3.571	1140	3.540
	Exp [e]	9–12	3910(560)	3.511(3)					1330(560)	3.542
	Exp [g]	7			2955(25)	3.5684(2)	1163(12)	3.6039(2)	1090(80)[h]	3.565[h]
	Exp [i]	8	2900(200)[j]	3.522[j]	2680(100)	3.5522(7)	1050(100)	3.5910(8)	950(80)[j]	3.551[j]
Atom	Ref	n	nf' $K'=5/2$				nf' $K'=7/2$			
			$J=2$		$J=3$		$J=3$		$J=4$	
			Γ_r	μ_ℓ	Γ_r	μ_ℓ	Γ_r	μ_ℓ	Γ_r	μ_ℓ
Ne	PF	15	23.15	0.0001	23.55	0.0001	9.612	0.0001	9.587	0.0001
	CI	12	20.32	0.00156	20.61	0.00158	8.69	0.00161	8.74	0.00163
	Exp [k]	12				0.0008(4)				
Ar	PF	20	191.4	0.0005	205.8	0.0009	79.1	0.0009	77.9	0.0008
	PF	9	185.7	0.0005	198.2	0.0009	76.9	0.0009	75.8	0.0008
	CI	9	181.8	0.00769	192.0	0.00792	80.9	0.00832	79.0	0.00824
	Exp [l]	9			166(3)	0.01122(3)				
	Exp [e]	10		0.010(5)	158(4)	0.01144(3)				0.010(5)
Kr	PF	20	286.1	0.0012	329.4	0.0019	154.2	0.0019	150.0	0.0017
	PF	5	226.8	0.0004	251.1	0.0011	141.0	0.0011	138.7	0.0010
	CI	11	251.8	0.0132	284.3	0.0138	151.2	0.0147	146.1	0.0144
	Exp [e]	5–7		0.011(4)						0.012(4)
	Exp [f]	8	301(20)							
Xe	PF	20	429.3	0.0034	593.4	0.0057	418.4	0.0057	398.6	0.0050
	PF	4	234.5	0.0012	292.3	0.0019	361.7	0.0019	355.2	0.0017
	CI	4	215.5	0.0167	271.9	0.0176	375.1	0.0186	364.4	0.0183
	Exp	4	210(20)[m]	0.0240(2)[m]	300(60)[i]	0.0259(6)[i]	251(31)[h]	0.025[h]	251(31)[h]	0.025 [h]

[a] Pauli-Fock calculation (Petrov et al. [11]). [b] CI≡CIPFCP (Configuration interaction Pauli-Fock calculation with inclusion of core polarization), present work. [c] One photon excitation from the metastable states (Peters et al. [14]). [d] Two-colour excitation from the Ne ground state (Petrov et al. [15]). [e] Four photon excitation from the ground state (Koeckhoven et al. [39]). [f] Present work; two-colour experiment (Orsay); $\Gamma_r\,(7f'[5/2]_2) = 243(40)$ cm^{-1}; $\Gamma_r\,(9f'[5/2]_2) = 356(40)$ cm^{-1}. [g] One photon excitation from the $6s'\ ^3P_0$ level (Kau et al. [40]). [h] One photon excitation from 5d- intermediate levels (Hanif et al. [27]). [i] One photon excitation from the $6s\ ^3P_2$ and the $6s'\ ^3P_0$ levels (Rundel et al. [26]); widths obtained by deconvolution, assuming Gaussian laser width of 4 cm^{-1} FWHM. [j] Two-colour experiment for $8p'$ resonance (Aloïse et al. [7]). [k] One photon excitation from the Ne($3s\ ^3P_2$) level (Peters et al., cited in [15]). [l] Present work; one photon excitation of $9f'$ resonance from the $3s\ ^3P_2$ metastable state (Kaiserslautern). [m] Two-colour experiment (Gisselbrecht et al. [6]).

$$4p^5_{3/2}5s\ ^3P_2 \xrightarrow{minor} \left\{ \begin{array}{l} 4p^5_{1/2}np'[1/2]_1\ \text{(iii)} \\ 4p^5_{1/2}np'[3/2]_1\ \text{(iv)} \\ 4p^5_{1/2}np'[3/2]_2\ \text{(v)} \\ 4p^5_{1/2}nf'[5/2]_2\ \text{(vi)} \\ 4p^5_{1/2}nf'[5/2]_3\ \text{(vii)} \\ 4p^5_{1/2}nf'[7/2]_3\ \text{(vii)} \end{array} \right\}. \qquad (14)$$

Transitions with conservation of the core angular momentum contain the single-electron amplitude. Therefore, the transitions described via the scheme (13) are denoted as the *major* transitions [28]. Transitions described via the scheme (14) are denoted as *minor* and contain only correlation amplitudes.

The theoretical lineshapes of the np'-resonances accessed from the metastable $(m+1)s'\ ^3P_0$ and $(m+1)s\ ^3P_2$ levels are depicted in Figure 1; experimental cross-sections (open circles) are included for the $^3P_2$ initial state [14].

For the $^3P_2$ levels, the non-resonant cross-section is always rather small and reflects the contribution from 10 channels (see [41]). The resonant contribution corresponds to the *minor* transitions in scheme (14) and is determined by the correlational amplitudes which contain energy integration over virtual states and thus depend rather weakly on energy. This behaviour is illustrated by the theoretical partial cross-sections $\sigma_{i_0}^{j_c=1/2;J}(\omega)$ above the $^2P_{1/2}$ threshold (chain lines in the right panels of Fig. 1). Moreover, the peak cross-sections for the *minor* transitions are quite similar for *all* Rg (about 2 to 4 Mb). The resonance structure of the $mp^5_{1/2}np'[K']_J$ ARS, excited from the respective $(m+1)s\ J_0=2$ level, contains three lines, as seen for Kr. Due to overlap, the three contributions are barely resolved in Ar and Xe.

For the $^3P_0$ levels, the size of the non-resonant cross-section mainly reflects the effect of s-d mixing in the initial states, thus explaining the high cross-section for Xe($^3P_0$) (see full line in Fig. 1c) whose wave function is given by [29]:

$$\left|5p^6 6s'\ ^3P_0\right\rangle = 0.7379\left|5p^5_{1/2}6s'\ ^3P_0\right\rangle - 0.6750\left|5p^5_{3/2}5d\ ^3P_0\right\rangle. \qquad (15)$$

For Ar and Kr, s-d mixing is distinctly smaller [41]. The strength of the ARS excited from the $^3P_0$ levels is dictated by the position of the respective Seaton-Cooper minima associated with a sign reversal in the single-electron transition moment $\langle(n/\varepsilon)\,p'\,|\mathbf{D}|\,(m+1)\,s'\rangle$ [42]. The shift of these minima towards higher energies from Ar to Xe (see right-hand panels of Fig. 1 where the partial cross-sections $\sigma_{i_0}^{j_c=1/2;J=1}$ for the *major* transitions are shown by solid lines above the respective $^2P_{1/2}$ threshold) leads to an increase of the oscillator strengths of the ARS from Ar to Xe.

The position of the Seaton-Cooper minimum is strongly sensitive to the correlations entering scheme (1) and to the core polarization potential, thus providing a sensitive test for many-electron theories. This sensitivity is illustrated in Figure 1a where we present by the dashed line the result of a calculation for the Ar $4s' \rightarrow 14p'[1/2,3/2]_1$ transitions with the core polarization potential for the 4s-electron decreased by a factor of 1.25. This decrease shifts the Seaton-Cooper minimum by 0.3 eV towards lower energies and reduces the oscillator strength for the $4s' \rightarrow 14p'[3/2]_1$ transition by about two orders of magnitude. As a consequence the composite $4s' \rightarrow 14p'[1/2]_1$ and $4s' \rightarrow 14p'[3/2]_1$ transitions exhibit a window profile due to the broader $14p'[1/2]_1$ resonance with a superimposed shoulder due to the sharp $14p'[3/2]_1$ resonance. In contrast, the experimental observation shows peak resonances [24,23]. We note that similar

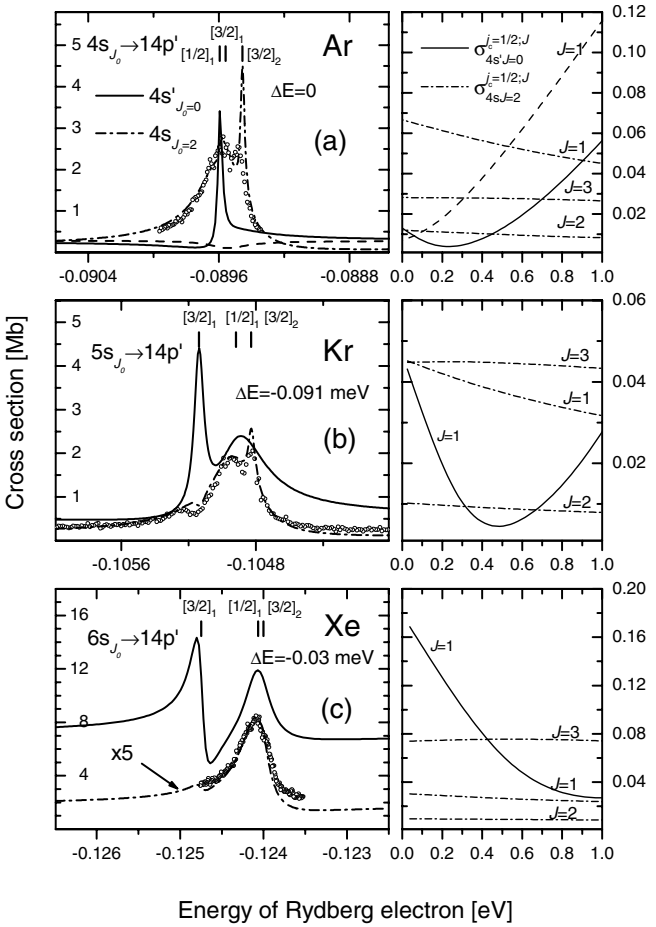

Fig. 1. Lineshapes of the autoionizing Rydberg series $mp^5_{1/2}np'$ of Ar, Kr and Xe excited from the metastable states $mp^5_{3/2}(m+1)s\ ^3P_2$ (chain lines) and $mp^5_{1/2}(m+1)s'\ ^3P_0$ (full lines). Partial cross-sections $\sigma_{i_0}^{j_c=1/2,J}(\omega)$ (Eq. (3)) are shown in the right hand panels. In order to facilitate comparison between experiment and theory experimental data from our earlier work [14] are normalized to the computed cross-sections and computed cross-sections are shifted by the ΔE documented in each panel. The dashed lines in the upper panels show the cross-sections for the $4s', J_0=0$ level computed with decreased core polarization potential (see text). The cross-sections, obtained within the velocity and length gauges, agree within 10%; therefore, only the results for the length gauge are shown.

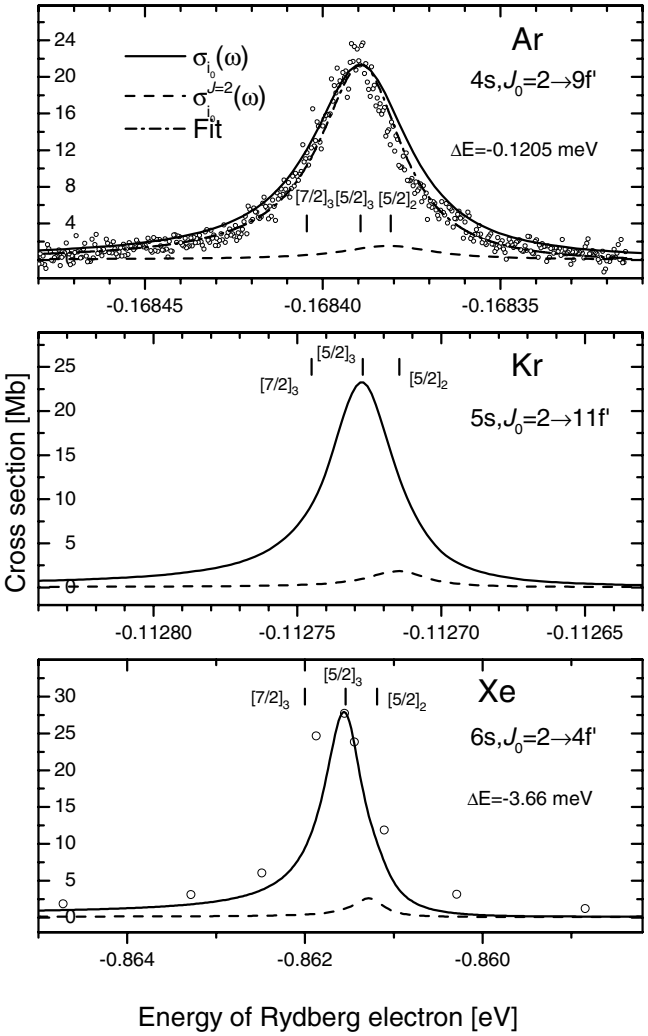

Fig. 2. Lineshapes of the Rydberg series $m\mathrm{p}^5_{1/2}n\mathrm{f}'$ of Ar, Kr and Xe excited from the metastable state $m\mathrm{p}^5_{3/2}\,(m+1)\,\mathrm{s}\ {}^3\mathrm{P}_2$. Experimental data for the $4\mathrm{s} \rightarrow 9\mathrm{f}'$ transition in Ar are from the present work and for the $6\mathrm{s} \rightarrow 4\mathrm{f}'$ transition in Xe are from [26] (UV bandwidth 0.5 meV). The dashed curves show the $J = 2$ partial cross-sections. In order to facilitate comparison between theory and experiment the computed energies are shifted by the ΔE documented in figure. The cross-sections, obtained within the velocity and length gauges, agree within 10%; therefore, only the results for the length gauge are shown.

changes of the Seaton-Cooper minimum can be obtained if the correlations ($1a$, $1d$) will be slightly scaled.

The major transitions $5\mathrm{s}' \rightarrow n\mathrm{p}'$ in Kr were measured by Dunning and Stebbings [23], but no substructure was observed (quoted resolution 1 meV). For Xe the major transitions $6\mathrm{s}' \rightarrow 7\mathrm{p}', 8\mathrm{p}'$ were investigated at high resolution by several groups (see [26,27,40] and references therein) with lineshapes similar to the theoretical prediction for the $6\mathrm{s}' \rightarrow 14\mathrm{p}'$ spectrum in Figure 1c.

The lineshapes of the $n\mathrm{f}'$-resonances accessed from the metastable ${}^3\mathrm{P}_2$ level are depicted in Figure 2. The positions of the three $n\mathrm{f}'$-resonances contributing to the cross-sections $\sigma_{(m+1)\mathrm{s}}\,(\omega)$ are indicated by vertical bars.

Table 3. Eigenvectors for the lowest excited states with $J_0 = 1$ in Ne, Ar, Kr and Xe.

Coupling	LS		$jj = jK$	
	$\vert{}^1\mathrm{P}_1\rangle$	$\vert{}^3\mathrm{P}_1\rangle$	$\vert 3/2, 1/2\rangle$	$\vert 1/2, 1/2\rangle$
Ne $\vert 3\mathrm{s}\rangle$	0.251	0.968	0.764	0.645
$\vert 3\mathrm{s}'\rangle$	0.968	−0.251	0.645	−0.764
Ar $\vert 4\mathrm{s}\rangle$	0.389	0.921	0.850	0.528
$\vert 4\mathrm{s}'\rangle$	0.921	−0.389	0.528	−0.850
Kr $\vert 5\mathrm{s}\rangle$	0.685	0.728	0.980	0.199
$\vert 5\mathrm{s}'\rangle$	0.728	−0.685	0.199	−0.980
Xe $\vert 6\mathrm{s}\rangle$	0.745	0.667	0.994	0.114

In addition, we show experimental spectra for Ar (this work) and Xe [26]. For all rare gases, the oscillator strength for the $(m+1)\,\mathrm{s}\ {}^3\mathrm{P}_2 \rightarrow n\mathrm{f}'[7/2]_3$ transition is several orders of magnitude smaller than that for the $(m+1)\,\mathrm{s}\ {}^3\mathrm{P}_2 \rightarrow n\mathrm{f}'[5/2]_3$ transition, and the resonance $n\mathrm{f}'[5/2]_2$ contributes only weakly to the cross-section (see dashed curves in Fig. 2). Therefore, the $n\mathrm{f}'$ resonance can be viewed as $n\mathrm{f}'[5/2]_3$ slightly broadened by $n\mathrm{f}'[5/2]_2$. The presently measured Ar $9\mathrm{f}'[5/2]_3$ resonance (open circles) and the fitted Fano profile (chain curve) are shown in the uppermost panel of Figure 2. Good agreement between the computed and measured lineshapes is observed. The experimental data for Xe($4\mathrm{f}'$) (open circles, taken from [26]) are broadened by the 0.5 meV photon bandwidth. Deconvolution of the widths, quoted in [26] for the $4\mathrm{f}'$ and $5\mathrm{f}'$ resonances, leads to a reduced widths of 300(60) cm^{-1} in agreement with the CIPFCP prediction (see Tab. 2).

4.2 Rg (np′, nf′) resonances accessed from several (ms, ms′, md) $J_0 = 1$ levels

The intermediate states $m\mathrm{p}^5\,(m+1)\,\mathrm{s}$ with total angular momentum $J_0 = 1$ have different representations in the different coupling schemes. We calculated the eigenvector for the lowest $m\mathrm{p}^5\,(m+1)\,\mathrm{s}$ $J_0 = 1$ states of Ar, Kr and Xe as described in our earlier paper for Ne [15], i.e. we solved the secular equation of the 88th order and renormalized the first two components because they contribute about 99% to the total eigenvector. The coefficients for the basis states in LS- and jj-coupling (the latter coincide with those of jK-coupling for the configuration $\mathrm{p}^5\mathrm{s}$) are listed in Table 3 where the results for Ne are included for completeness. The Ne eigenvectors are better described by LS-coupling whereas for Kr and Xe jj-coupling is preferable because of the increased spin-orbit interaction of the mp core electron. Ar represents the case of intermediate coupling. In Table 3 we omit the eigenvector for the upper $6\mathrm{s}'$ level of Xe, because it exhibits strong s–d mixing. The corresponding eigenvector is given by:

$$|6\mathrm{s}'\rangle = 0.503\,|6\mathrm{s}\ {}^1\mathrm{P}_1\rangle - 0.353\,|6\mathrm{s}\ {}^3\mathrm{P}_1\rangle - 0.078\,|5\mathrm{d}\ {}^1\mathrm{P}_1\rangle + 0.769\,|5\mathrm{d}\ {}^3\mathrm{P}_1\rangle - 0.154\,|5\mathrm{d}\ {}^3\mathrm{D}_1\rangle\,. \quad (16)$$

The ARS, which are accessible from the $J_0 = 1$ levels, are summarized in the following scheme (again given only for

the case of Kr):

$$4p^5_{j_c}\,5s\ J=1 \rightarrow \left\{ \begin{array}{l} 4p^5_{1/2}np'[1/2]_0\ \text{(i)} \\ 4p^5_{1/2}np'[1/2]_1\ \text{(ii)} \\ 4p^5_{1/2}np'[3/2]_1\ \text{(iii)} \\ 4p^5_{1/2}np'[3/2]_2\ \text{(iv)} \\ 4p^5_{1/2}nf'[5/2]_2\ \text{(v)} \end{array} \right\}. \qquad (17)$$

Excitation of the ARS via the $J_0 = 1$ intermediate levels accesses all four $4p^5_{1/2}np'$ series. In addition the series $4p^5_{1/2}nf'[5/2]_2$ can be observed as isolated resonances. For Ne and Ar, the $nf'[5/2]_2$ ARS are predicted to exhibit near-Lorentzian shapes with high q-parameters. For Ne this series has been observed [15], but the experimental resolution was insufficient to determine the width and the shape of the resonances. For Xe, good agreement between the measured [6] and computed line profiles of the $4f'[5/2]_2$ resonance (excited via the $5d[3/2]_1$ level) has been observed [22]. New results for the Kr($8f'[5/2]_2$) resonance are reported below.

The computed cross-sections for the np' resonances involving the *minor* ($j_c = 3/2$) and *major* ($j_c = 1/2$) transitions from the lowest $J_0 = 1$ levels of Ar, Kr and Xe are depicted in Figure 3. In the right-hand panels of this figure the partial cross-sections $\sigma_{i_0}^{j_c=1/2;J}(\omega)$ are shown. Extrapolation of these cross-sections to negative energies yields an estimate of the peak cross-sections in the respective Rydberg series.

The relative values of the spin-orbit interaction of the mp core electron and the $mp - np$ Coulomb interaction between Rydberg electron and the core change considerably from Ne to Xe. As a result, the energetic sequence of the $[1/2]_1$ and $[3/2]_1$ resonances changes from Ar to (Kr, Xe), and the $[1/2]_1$ and $[3/2]_2$ resonances form the closest pair for Kr and Xe. The broad resonance $np'[1/2]_0$ is well separated from the other resonances and dominates the cross-sections for the *major* transition in Ar and Kr. In Xe, s–d mixing increases the oscillator strength for the transitions to the $J = 1, 2$ resonances and the non-resonant cross-sections to the $mp^5_{3/2}\varepsilon fJ$ continua.

Figure 3 illustrates that the $np'[1/2]_0$ resonances have strongly different lineshapes when accessed from the $(m+1)\,s\ ^3P_1$ and $(m+1)\,s'\ ^1P_1$ levels. For Ne [15] we found that the difference results from the interference between the direct $3s \rightarrow np'$ transition and the correlational transitions $3s \rightarrow \{p\} \Longrightarrow np'$ which involve virtual excitations to all intermediate $2p^5\{p\}$ configurations (see also correlation f in scheme (1)). The $3s \rightarrow 3p \Longrightarrow np'$ pathway contributes about 50% of the total correlation $(1f)$ because of the high strength of the $3s \rightarrow 3p$ dipole amplitude. The interference arises from the mixing of the core states $2p^5_{1/2}$ and $2p^5_{3/2}$ with different angular momentum j_c by the Coulomb interaction with the 3s electron in the intermediate state and with the Rydberg np' electron in the final state.

In order to clarify the influence of these virtual $(m+1)\,s \rightarrow (m+1)\,p \Longrightarrow np'$ transitions on the ARS shown in Figure 3, we performed an exploratory calculation for Ar, excluding the pathway $4s \rightarrow 4p \Longrightarrow np'$ from the correlation $(1f)$. The results of this calculation are presented in Figure 4 by dashed curves in comparison with the complete calculations, shown by the solid lines. The cross-sections computed without the $4s \rightarrow 4p \Longrightarrow np'$ excitation pathway exhibit nearly the same peak value for the 4s and 4s′ intermediate levels in the region of the $14p'[1/2]_0$ resonance (cf. Figs. 4a and 4b; note the different cross-section scales). As in Ne [15] interference between the direct and the virtual excitation channels is destructive for the Ar(4s) intermediate level and constructive for the Ar(4s′) level. As a consequence, the $14p'[1/2]_0$ resonance is strongly reduced in the cross-sections $\sigma_{4s\ J_0=1}(\omega)$ while it is even more prominent in the cross-section $\sigma_{4s'\ J_0=1}(\omega)$. Other resonances excited from the intermediate levels with $J_0 = 1$ are also strongly influenced by the $4s \rightarrow 4p \Longrightarrow np'$ pathway (cf. Figs. 4a and 4b).

For a more detailed comparison we show also the influence of the virtual excitations on the np' resonances for excitation from the metastable $J_0 = 2$ (Fig. 4d) and

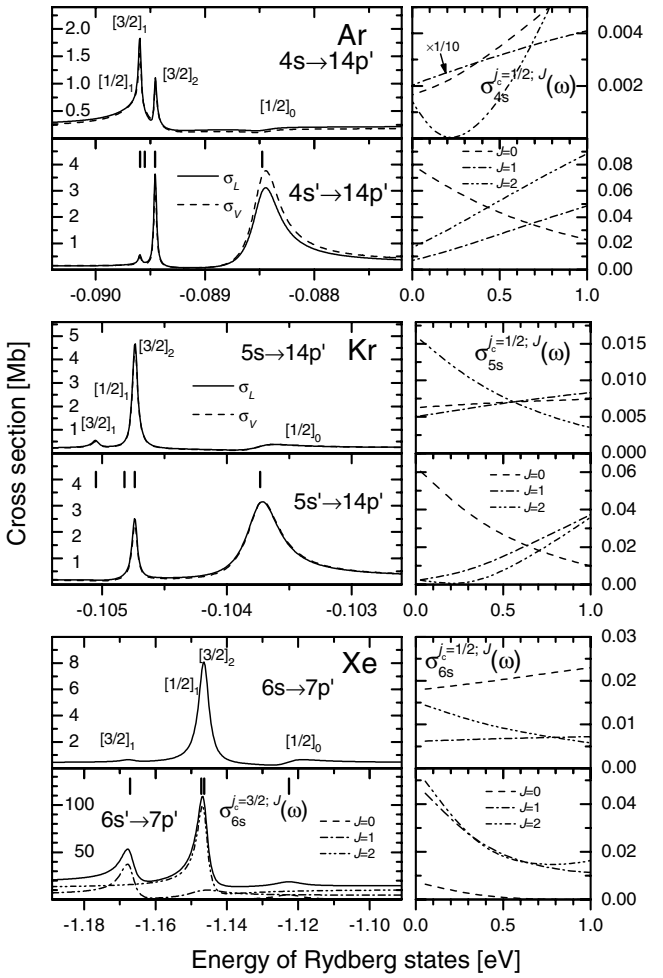

Fig. 3. Lineshapes of the Rydberg series $mp^5_{1/2}np'$ of Ar, Kr and Xe accessed from the lowest intermediate states $mp^5_{3/2}\,(m+1)\,s$ $(J_0 = 1)$ and $mp^5_{1/2}\,(m+1)\,s'$ $(J_0 = 1)$. In the right hand panels the partial cross-sections $\sigma_{i_0}^{j_c=1/2,J}(\omega)$ are shown.

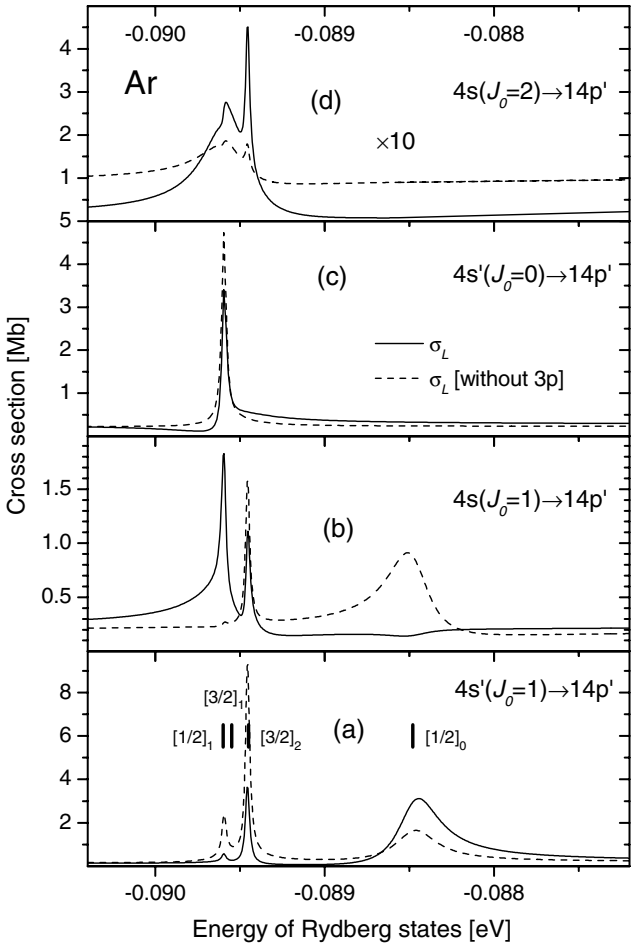

Fig. 4. Comparison of the Ar cross-sections at the range of 14p′ resonance computed with (solid line) and without (dashed line) taking into account excitation of the 14p′ resonance through virtual 4p shell.

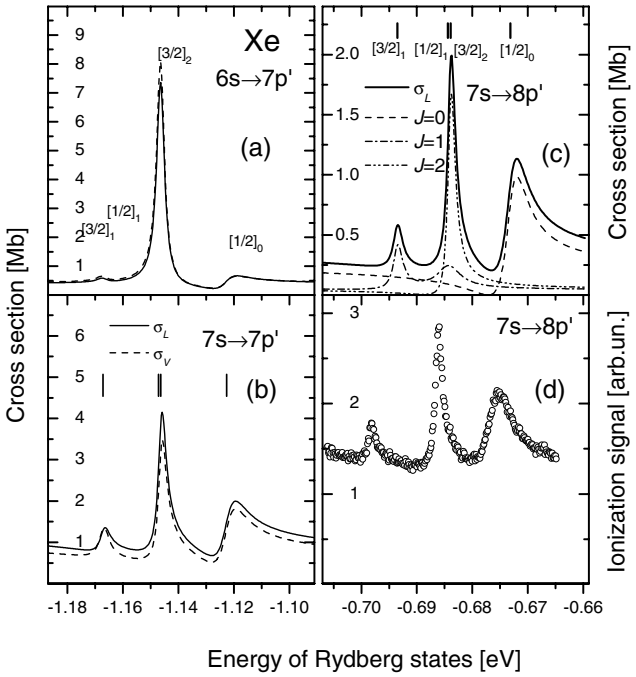

Fig. 5. Lineshapes of the Xe(np') resonances accessed from the $ms\ ^3P_1$ intermediate levels. Results of the present two-colour experiment are depicted in panel (d). In panel (c) the partial cross-sections for $J = 0, 1, 2$ are also illustrated.

$J_0 = 0$ (Fig. 4c) levels. When the np' resonances are excited from the $3p^5_{3/2}4s$ ($J_0 = 2$) metastable level the virtual channel $4s \rightarrow 4p \Longrightarrow np'$ is the dominant excitation mechanism. The neglect of the virtual excitation channel reduces the photoionization cross-sections by an order of magnitude (see Fig. 4d).

The interference between the direct $ks \rightarrow np'$ and the virtual $ks \rightarrow kp \Longrightarrow np'$ channels depends on the amplitudes of the $mp^5_{1/2}ks$ and $mp^5_{3/2}ks$ configurations in the total wave function of the initial state. These amplitudes are changed when the spin-orbit interaction for the mp electron is changed (for atoms with different Z, see Tab. 3) or the $mp - ks$ Coulomb interaction is changed (for different intermediate ks-levels). The latter effect is illustrated in the left-hand panels of Figure 5 where the photoionization cross-sections $\sigma_{6s}(\omega)$ and $\sigma_{7s}(\omega)$ are compared in the range of the 7p′ resonance. As compared to $5p^56s$, the $5p^57s$ configuration is closer to jj coupling, and the destructive interference between the direct and virtual excitation channels for the configuration $5p^5_{3/2}7s$ is smaller than for the configuration $5p^5_{3/2}6s$. Correspondingly, the $7p'[1/2]_0$ resonance is stronger in $\sigma_{7s}(\omega)$ than in $\sigma_{6s}(\omega)$. Theory predicts the next member of the Rydberg series $8p'[1/2]_0$, excited from the 7s intermediate level, to be even more prominent (see Fig. 5c).

The experimental resonance profiles for the $7s \rightarrow 8p'$ transition in Xe are shown in Figure 5d. The data have been obtained by the two-colour technique described in Section 2.2. The isotropic cross-section has been obtained here by setting the relative orientation between the electric field vectors of the linearly polarized synchrotron and laser radiation to the 'magic' angle θ_{mag}. Good agreement is found for the lineshapes and relative intensities of the $7s \rightarrow 8p'$ resonances when comparing measured and computed data (Figs. 5c, 5d). The main difference is related to the non-resonant ionization cross-section, which is much larger in the experiment than in theory. Part of this difference might be due to a not completely reduced background in the experimental data arising from photoionization events already produced without the ionizing laser. But even by taking into account this experimental uncertainty, the introduced corrections cannot explain the observed discrepancy between theory and experiment and further investigations are needed for clarification.

The computed partial cross-sections $\sigma_{7s}^{j_c=3/2;J}(\omega)$ for the 8p′ resonances are depicted in Figure 5c. The rather weak and broad $np'[1/2]_1$ resonance is superimposed by the intense $np'[3/2]_2$ resonance. Theory predicts a reduced width of 3627 cm^{-1} for the $8p'[1/2]_1$ resonance (Tab. 2), which is closer to the experimental value 2680(100) cm^{-1} (obtained by deconvolution of the width reported in [26]), but much larger than the width 1560(460) cm^{-1} obtained

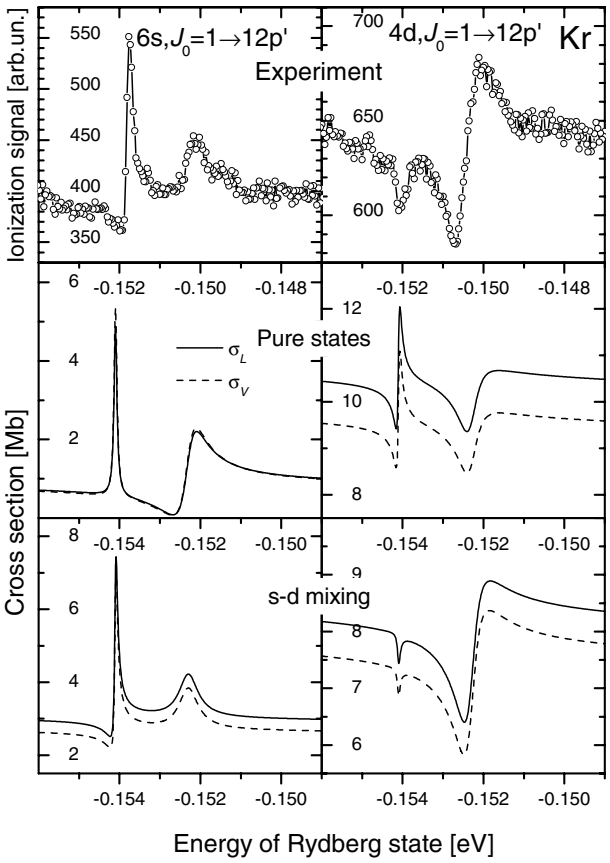

Fig. 6. Influence of s − d mixing on the 6s/4d $J_0 = 1 \rightarrow 12p'$ transitions in Kr. The middle panels correspond to the calculations with the 'pure' $4p^5_{3/2}6s$- and $4p^5_{3/2}4d$-states. The low panels correspond to calculations with inclusion of the interaction between the $4p^5_{3/2}6s$- and $4p^5_{3/2}$ 4d-configurations. All spectra correspond to parallel linear polarization of the exciting and ionizing radiation.

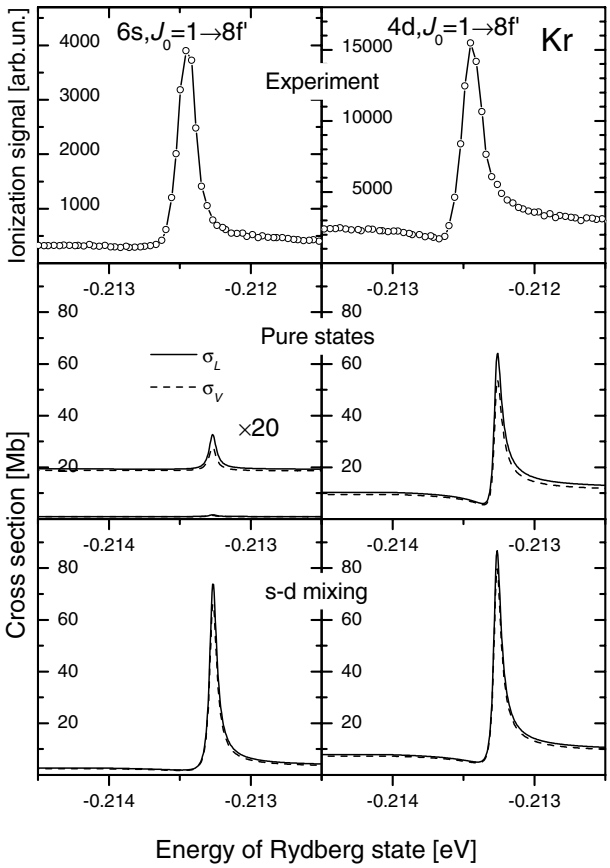

Fig. 7. Influence of s − d mixing on the 6s/4d $(J_0 = 1) \rightarrow 8f'$ transition in Kr. The middle panels correspond to the calculations with 'pure' $4p^5_{3/2}6s$- and $4p^5_{3/2}4d$-states. The low panels correspond to calculations with inclusion of the interaction between the $4p^5_{3/2}6s$- and $4p^5_{3/2}4d$-configurations. All spectra correspond to parallel linear polarization of the exciting and ionizing radiation.

in [7] as a result of a deconvolution procedure applied to measurements of the linear and circular dichroism.

The uppermost panels of Figures 6 and 7 show the measured cross-sections for the Kr $(6s/4d \rightarrow 12p')$ and Kr $(6s/4d \rightarrow 8f')$ transitions, respectively. In these measurements parallel linear polarizations of the exciting and ionizing radiation were used, thus suppressing the $np'[K]_1$ resonances [10]. In order to extract the lineshape parameters we have performed a Fano-profile analysis. During the fitting procedure a convolution with a triangular function was included, which accounts in a simple way for the broadening of the line due to the spectral width of the laser. The experimental reduced widths of the p′- and f′-resonances agree with the computed values within the error bars (see Tab. 2).

In the middle panels of Figures 6 and 7 we depict the results of calculations when the wave functions of the 6s/4d $J_0 = 1$ intermediate levels are considered as 'pure' basis states in jK-coupling (the parallel polarization arrangement of the exciting and ionizing radiation was accounted for by using Eq. (5) with $\theta = 0°$). The jK-eigenvectors are given by:

$$|6s[3/2]_1\rangle = 0.795\,|6s\ ^1P_1\rangle + 0.606\,|6s\ ^3P_1\rangle \quad (18)$$

$$|4d[3/2]_1\rangle = 0.770\,|4d\ ^1P_1\rangle - 0.036\,|4d\ ^3P_1\rangle - 0.636\,|4d\ ^3D_1\rangle\,. \quad (19)$$

The resulting theoretical spectra differ strongly from those observed experimentally: (i) the computed cross-section for the $6s \rightarrow 8f'$ transition is far too small; (ii) in contrast to the experimental data for the $6s \rightarrow 12p'$ transition, the calculated cross-section exhibits a too low 'background'; (iii) large differences between the theoretical and experimental lineshapes of the $4d \rightarrow 12p'$ transition are observed.

In view of the proximity of the 6s $J_0 = 1$ and 4d $J_0 = 1$ levels, we computed new wave functions, taking into

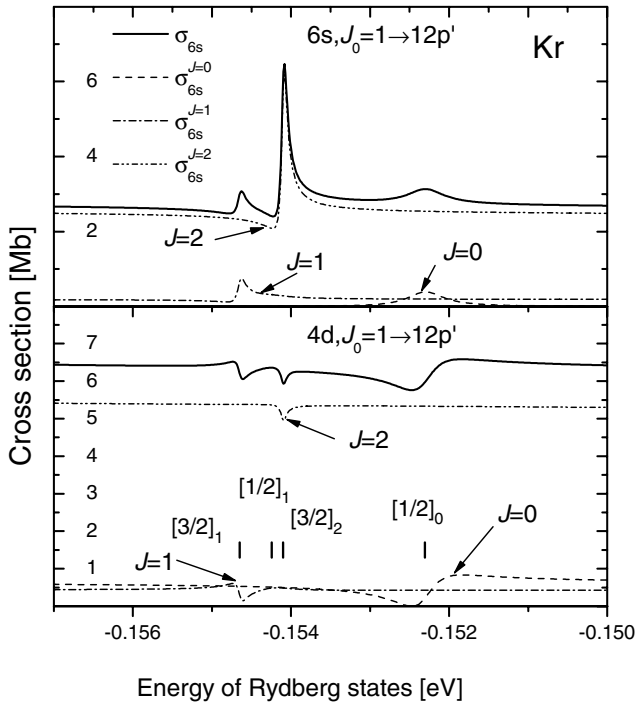

Fig. 8. Isotropic cross-sections $\sigma_{6s}(\omega)$ and $\sigma_{4d}(\omega)$ in the range of the Kr(12p′) resonance. Partial cross-sections $\sigma_{i_0}^{J}(\omega)$ (Eq. (3)) are also shown.

account s–d mixing. The resulting eigenvectors are given by:

$$\begin{aligned}|6s_{J_0=1}\rangle &= 0.643\,|6s\ ^1P_1\rangle + 0.491\,|6s\ ^3P_1\rangle \\ &\quad -0.454\,|4d\ ^1P_1\rangle + 0.129\,|4d\ ^3P_1\rangle \\ &\quad +0.351\,|4d\ ^3D_1\rangle \qquad (20)\\ |4d_{J_0=1}\rangle &= 0.596\,|4d\ ^1P_1\rangle \\ &\quad +0.026\,|4d\ ^3P_1\rangle - 0.559\,|4d\ ^3D_1\rangle \\ &\quad +0.461\,|6s\ ^1P_1\rangle + 0.346\,|6s\ ^3P_1\rangle\,. \qquad (21)\end{aligned}$$

Using these eigenvectors, the spectra in the lowest panels in Figures 6 and 7 were obtained; they show very good overall agreement with the experimental observations.

The total isotropic cross-sections computed via equation (2) for the Kr (6s/4d → 12p′) transitions are depicted in Figure 8 together with the partial cross-sections given by equation (3). The total cross-sections clearly exhibit the $np'[3/2]_1$ resonance on the low-energy side of the spectra. The broad resonance $np'[1/2]_1$ can only be weakly seen in the partial cross-section $\sigma_{6s}^{j_c=3/2;J}(\omega)$ where it appears as a long high-energy tail of the $np'[3/2]_1$ resonance. Careful inspection of the measured spectra for the Kr (6s/4d → 12p′) transitions (upper panels in Fig. 6) indicates traces of the $np'[3/2]_1$ resonance which may arise from hyperfine induced depolarization effects for ^{83}Kr and/or a small deviation from parallel linear polarizations of the two light fields.

5 Summary

The narrow $Ar(3p_{1/2}^5 nf')$ autoionizing resonances were measured by single photon excitation of metastable $Ar(4s\ ^3P_2)$ atoms with a pulsed frequency-doubled dye laser (bandwidth 0.004 cm^{-1}) in conjunction with time-of-flight ion detection. Two-colour experiments, combining synchrotron radiation for exciting the $4p_{3/2}^5$ (6s/4d) and $5p_{3/2}^5$7s intermediate states and light from a linear dye laser for resonant ionization, were used to study the $Kr(12p'/8f'[K']_J)$ and $Xe(8p'[K']_J)$ autoionizing resonances. Lineshape parameters for all these resonances have been derived by a Fano-type analysis, thus yielding reduced resonance widths.

The experimental spectra and the resonance parameters are compared with theoretical calculations which are based on the configuration interaction Pauli–Fock approach, including core polarization. Computed and measured reduced widths and quantum defects for the even parity resonances are found to be in a good overall agreement. Lineshapes for the $(m+1)\,s/(m+1)\,s'$ $J_0 = 1 \rightarrow np'$ transitions are predicted for the resonance levels in Ar, Kr, Xe ($m = 3, 4, 5$). Some of the partial cross-sections exhibit a Seaton-Cooper minimum, thus providing a sensitive test of the theoretical approach. The cross-sections for the Kr (6s/4d → 12p′) and Kr (6s/4d → 8f′) transitions strongly depend on the s–d mixing in the intermediate state, thus providing a good test of the computed eigenvectors of these states. Strong effects due to the competition and interference between direct excitation of the autoionizing resonances and their excitation via virtual intermediate channels are revealed.

This work was supported by the Deutsche Forschungsgemeinschaft (436 RUS 17/55/05 and 436 RUS 17/05/06) and by the Forschungszentrum *Optische Technologien und Lasergesteuerte Prozesse*. IDP and VLS acknowledge the hospitality of the Fachbereich Physik at the Universität Kaiserslautern.

References

1. H. Beutler, Z. Phys. **93**, 177 (1935)
2. J. Berkowitz, *Photoabsorption, Photoionization and Photoelectron Spectroscopy* (Academic Press, New York, 1979)
3. R.F. Stebbings, F.B. Dunning, R.D. Rundel, in *Atomic Physics*, edited by G. Putlitz, E.W. Weber, A. Winnacker (Plenum Press, New York, 1975), Vol. 4, pp. 713–730
4. J. Berkowitz, Adv. Chem. Phys. **72**, 1 (1988)
5. H. Hotop, D. Klar, S. Schohl, in *Resonance Ionization Spectroscopy, Inst. Phys. Conf.*, edited by C.M. Miller, J.E. Parks (IOP Publishing, Bristol, 1992), Vol. 128, p. 45
6. M. Gisselbrecht, A. Marquette, M. Meyer, J. Phys. B: At. Mol. Opt. Phys. **31**, L977 (1998)
7. S. Aloïse, P. O'Keeffe, D. Cubaynes, M. Meyer, A.N. Grum-Grzhimailo, Phys. Rev. Lett. **94**, 223002 (2005)
8. W.R. Johnson, M. LeDourneuf, J. Phys. B: At. Mol. Opt. Phys. **13**, L13 (1980)

9. W.R. Johnson, K.T. Cheng, K.N. Huang, M. LeDourneuf, Phys. Rev. A **22**, 989 (1980)
10. D. Klar, K. Harth, J. Ganz, T. Kraft, M.W. Ruf, H. Hotop, V. Tsemekhman, K. Tsemekhman, M.Y. Amusia, Z. Phys. D **23**, 101 (1992)
11. I.D. Petrov, V.L. Sukhorukov, H. Hotop, J. Phys. B: At. Mol. Opt. Phys. **35**, 323 (2002)
12. I.D. Petrov, V.L. Sukhorukov, H. Hotop, J. Phys. B: At. Mol. Opt. Phys. **36**, 119 (2003)
13. M. Hanif, M. Aslam, R. Ali, S.A. Bhatti, M.A. Baig, D. Klar, M.W. Ruf, I.D. Petrov, V.L. Sukhorukov, H. Hotop, J. Phys. B: At. Mol. Opt. Phys. **37**, 1987 (2004)
14. T. Peters, T. Halfmann, U. Even, A. Wünnenberg, I.D. Petrov, V.L. Sukhorukov, H. Hotop, J. Phys. B: At. Mol. Opt. Phys. **38**, S51 (2005)
15. I.D. Petrov, V.L. Sukhorukov, T. Peters, O. Zehnder, H.J. Wörner, F. Merkt, H. Hotop, J. Phys. B: At. Mol. Opt. Phys. B **39**, (2006, accepted)
16. U. Fano, Phys. Rev. **124**, 1866 (1961)
17. U. Fano, J.W. Cooper, Phys. Rev. **137**, A1364 (1965)
18. K.T. Taylor, N.S. Scott, J. Phys. B: At. Mol. Phys. **14**, L237 (1980)
19. V. Radojevic, J.D. Talman, J. Phys. B: At. Mol. Opt. Phys. **23**, 2241 (1990)
20. V. Tsemekhman, K. Tsemekhman, M. Amusia, in *Resonance Ionization Spectroscopy*, *Inst. Phys. Conf.*, edited by C.M. Miller, J.E. Parks (IOP Publishing, Bristol, 1992), Vol. 128, p. 79
21. V. Tsemekhman, K. Tsemekhman, M. Amusia, in *Resonance Ionization Spectroscopy*, *Inst. Phys. Conf.*, edited by C.M. Miller, J.E. Parks (IOP Publishing, Bristol, 1992), Vol. 128, p. 83
22. M. Meyer, M. Gisselbrecht, A. Marquette, C. Delisle, M. Larzillière, I.D. Petrov, N.V. Demekhina, V.L. Sukhorukov, J. Phys. B: At. Mol. Opt. Phys. **38**, 285 (2005)
23. F.B. Dunning, R.F. Stebbings, Phys. Rev. A **9**, 2378 (1974)
24. R.F. Stebbings, F.B. Dunning, Phys. Rev. A **8**, 665 (1973)
25. R.F. Stebbings, C.L. Latimer, W.P. West, F. Dunning, T.B. Cook, Phys. Rev. A **12**, 1453 (1975)
26. R. Rundel, F. Dunning, H.C.J. Goldwire, R.F. Stebbings, J. Opt. Soc. Am. **65**, 628 (1975)
27. M. Hanif, M. Aslam, M. Riaz, S.A. Bhatti, M.A. Baig, J. Phys. B: At. Mol. Opt. Phys. **38**, S65 (2005)
28. R. Kau, I.D. Petrov, V.L. Sukhorukov, H. Hotop, J. Phys. B: At. Mol. Opt. Phys. **29**, 5673 (1996)
29. R. Kau, I.D. Petrov, V.L. Sukhorukov, H. Hotop, Z. Phys. D **39**, 267 (1997)
30. J. Bömmels, J.M. Weber, A. Gopalan, N. Herschbach, E. Leber, A. Schramm, K. Ueda, M.W. Ruf, H. Hotop, J. Phys. B: At. Mol. Opt. Phys. **32**, 2399 (1999)
31. L. Nahon, C. Alcaraz, J.L. Marlats, B. Lagarde, F. Polack, R. Thissen, D. Lepere, K. Ito, Rev. Sci. Instrum. **72**, 1320 (2001)
32. I.D. Petrov, V.L. Sukhorukov, H. Hotop, J. Phys. B: At. Mol. Opt. Phys. **32**, 973 (1999)
33. I.D. Petrov, V.L. Sukhorukov, E. Leber, H. Hotop, Eur. Phys. J. D **10**, 53 (2000)
34. A.F. Starace, *Theory of atomic photoionization*, *Handbuch der Physik* (Springer, Berlin, 1982), Vol. 31
35. S.L. Sorensen, T. Åberg, J. Tulkki, E. Rachlew-Kallne, G. Sundstrom, M. Kirm, Phys. Rev. A **50**, 1218 (1994)
36. B.W. Shore, Phys. Rev. **171**, 43 (1968)
37. B.R. Judd, *Second quantization and atomic spectroscopy* (John Hopkins, Baltimore, 1967)
38. I. Lindgren, J. Morrison, *Atomic many-body theory*, *Chemical physics* (Springer-Verlag, Berlin, 1982), Vol. 13
39. S.M. Koeckhoven, W.J. Buma, C.A. de Lange, Phys. Rev. A **51**, 1097 (1995)
40. R. Kau, D. Klar, S. Schohl, S. Baier, H. Hotop, Z. Phys. D **36**, 23 (1996)
41. R. Kau, I.D. Petrov, V.L. Sukhorukov, H. Hotop, J. Phys. B: At. Mol. Opt. Phys. **31**, 1011 (1998)
42. M.J. Seaton, Proc. R. Soc. A **208**, 418 (1951)